

Dynamic reorganization of intrinsic functional networks in the mouse brain



Joanes Grandjean^a, Maria Giulia Preti^{b,c}, Thomas A.W. Bolton^{b,c}, Michaela Buerge^d,
Erich Seifritz^{e,f}, Christopher R. Pryce^{d,f}, Dimitri Van De Ville^{b,c}, Markus Rudin^{a,f,g,*}

^a Institute for Biomedical Engineering, University and ETH Zurich, Zurich, Switzerland

^b Institute of Bioengineering, École Polytechnique Fédérale de Lausanne (EPFL), Lausanne, Switzerland

^c Department of Radiology and Medical Informatics, University of Geneva, Geneva, Switzerland

^d Preclinical Laboratory for Translational Research into Affective Disorders, DPPP, Psychiatric Hospital, University of Zurich, Zurich, Switzerland

^e Department of Psychiatry, Psychotherapy and Psychosomatics (DPPP), Psychiatric Hospital, University of Zurich, Zurich, Switzerland

^f Neuroscience Center Zurich, University of Zurich and ETH Zurich, Zurich, Switzerland

^g Institute of Pharmacology and Toxicology, University of Zurich, Zurich, Switzerland

ARTICLE INFO

Keywords:

Mouse
fMRI
Functional connectivity
Dynamic functional states
Dictionary learning

ABSTRACT

Functional connectivity (FC) derived from resting-state functional magnetic resonance imaging (rs-fMRI) allows for the integrative study of neuronal processes at a macroscopic level. The majority of studies to date have assumed stationary interactions between brain regions, without considering the dynamic aspects of network organization. Only recently has the latter received increased attention, predominantly in human studies. Applying dynamic FC (dFC) analysis to mice is attractive given the relative simplicity of the mouse brain and the possibility to explore mechanisms underlying network dynamics using pharmacological, environmental or genetic interventions. Therefore, we have evaluated the feasibility and research potential of mouse dFC using the interventions of social stress or anesthesia duration as two case-study examples. By combining a sliding-window correlation approach with dictionary learning, several dynamic functional states (dFS) with a complex organization were identified, exhibiting highly dynamic inter- and intra-modular interactions. Each dFS displayed a high degree of reproducibility upon changes in analytical parameters and across datasets. They fluctuated at different degrees as a function of anesthetic depth, and were sensitive indicators of pathology as shown for the chronic psychosocial stress mouse model of depression. Dynamic functional states are proposed to make a major contribution to information integration and processing in the healthy and diseased brain.

Introduction

Functional connectivity (FC) is a measure of statistical interdependence of the activity traces of two brain regions, providing insight into interactions between brain areas and how they jointly support information processing (Power et al., 2014). FC analysis has gained in importance over the past decade, shedding light on large-scale brain organization by identifying a set of autonomous network modules such as the default mode network (DMN), and contributing to improved understanding of brain function and the changes underlying several brain disorders (Greicius, 2008). While information processing by the brain is a highly dynamic process requiring exquisitely orchestrated regional interactions, the majority of FC studies on spontaneous brain activity as assessed by functional magnetic resonance imaging (fMRI) assume stationarity, i.e. constant interactions throughout the duration of a resting-state scanning session. However, rapid changes in EEG microstate, i.e. coherent activation at a sub-second time scale

within global functional brain networks, have been described (Van de Ville et al., 2010). Dynamic functional connectivity (dFC) aims to capture aspects of time-varying coupling patterns between regions and therefore to reveal the dynamic features of network organization. Interestingly, dynamic EEG microstates have been shown to correlate significantly with activity in fMRI resting-state networks despite the pronounced temporal filtering imposed by the hemodynamic response function (Van de Ville et al., 2010).

A wide range of approaches has been used to analyze the dynamic characteristics of the fMRI signal (Calhoun et al., 2014). Changes in FC across time can be estimated by applying a so-called *sliding-window* approach, in which the resting-state brain signals are subdivided into time-shifted segments of short duration, each of which then undergoes correlation analysis. For studies considering more than a few pairwise interactions or aiming at group-level analysis, dimensionality reduction is commonly achieved by applying multivariate techniques to the large set of FC time courses. Allen and colleagues proposed the application of

* Correspondence to: Institute for Biomedical Engineering, University and ETH Zürich, AIC-ETH HCI D426, Vladimir-Prelog-Weg 4, CH-8093 Zürich, Switzerland.
E-mail address: rudin@biomed.ee.ethz.ch (M. Rudin).

k-means clustering to identify dynamic functional states (dFS) (Allen et al., 2014), while previous work by Leonardi et al. introduced eigennconnectivities by the application of principal component analysis (PCA) (Leonardi et al., 2013), and dictionary learning (Leonardi et al., 2014).

The dynamic nature of FC raises questions concerning the neuronal basis underlying this phenomenon, both in the normal and diseased brain. It has been suggested that dynamic FC patterns in awake humans at rest might be driven by both conscious and unconscious brain processes, which may vary across subjects (Hutchison et al., 2013), rendering the elucidation of mechanistic aspects difficult. Analogous studies in anesthetized animals serve as a powerful complementary approach to gain mechanistic insight. Hutchison et al. demonstrated the non-stationary behaviour of FC in anesthetized monkeys, proving the existence of dFS in the unconscious brain and in the absence of potential confounds due to head motion (Hutchison et al., 2013). Analysis of the dynamic properties of FC in anesthetized rats revealed similarities with dFC patterns in awake humans and monkeys (Majeed et al., 2011), and furthermore demonstrated a correlation between dFS derived from resting-state fMRI and the dynamics of electrophysiological recordings (Thompson et al., 2013). Studies in mice offer additional opportunities to examine factors regulating dFC aspects. Optogenetics (Lee et al., 2010) and pharmacological interventions (Razoux et al., 2013) may be used to modulate specific neuronal populations in order to analyze their involvement in wide-range neural networks and in dynamic network interactions. In addition, models of human pathology might indicate disease-specific alterations in dFC, which could be relevant from a mechanistic point of view or serve as early disease indicators (Grandjean et al., 2014b).

We have evaluated whether dFC analysis of anesthetized mice resting-state fMRI data enables the identification of dFS that is sufficiently reproducible to study potential alterations due to changes in physiological conditions or in response to pathological stress. The results are organized into four sections: i) quality control with regard to reproducibility of brain parcellation and stationary FC analysis, ii) estimation of reference dFS based on rs-fMRI data of healthy mice, iii) a test of dFC on surrogate data, as well as of the reproducibility and generalization of dFS in an independent dataset, and iv) analysis of the sensitivity of the approach in identifying dFC changes induced by pathology (murine model of chronic psychosocial stress) or alterations in physiological state (prolonged anaesthesia).

Stationary FC analysis revealed a segregated organization into distinct modules such as the sensory-motor cortical networks, sub-cortical networks, and DMN. To establish meaningful group-level components of fluctuations of FC, we applied dictionary learning to the dFC time courses obtained with sliding-window correlation. This method allows for generalization upon conventional subspace methods such as PCA and ICA by adding constraints such as temporal sparsity, bounded values, and positivity (Leonardi et al., 2014). The positivity constraint allows for discrimination of increases and decreases in connectivity, so that these are not forced to have the same temporal occurrence for the whole duration of data acquisition. Furthermore, positivity enables the capturing of strongly anti-correlated patterns as two different building blocks with anti-correlated time courses. Inclusion of temporal sparsity can be justified in view of a recent report providing evidence that the various networks are acting together, but not the whole repertoire at once (Karahanoglu and Van De Ville, 2015). This indicates that connectivity states exist economically, with only a subset being active together at a given time point.

The dFC analysis revealed dynamic interactions between and within the modules derived by stationary FC analysis. Furthermore, we show that the patterns identified by dictionary learning could be reproduced in an independent dataset using a different preprocessing pipeline, and that they are largely independent of parameter choices throughout the analytical procedure. Finally, we demonstrate that dFS might constitute sensitive indicators of: abnormal processing, as illustrated in a

mouse model of psychosocial stress-induced depression-like brain and behaviour (Azzinnari et al., 2014; Grandjean et al., 2016a); and physiological adaptations, as observed during prolonged anaesthesia. The data show that dFC analysis identifies rich information on functional brain organization that remains hidden under conventional stationary FC approaches. Overall, we demonstrate that dFC analysis constitutes a number of promising research avenues with practical guidelines that can lead to better and more sensitive imaging-based biomarkers.

Materials and methods

Animals and preparation

All experiments were conducted following the Swiss federal ordinance for animal experimentation, and were licensed by the Zürich cantonal veterinary office. A total of 92 C57BL/6 mice bred in-house, 14 females and 78 males aged 8–12 weeks, were studied. Animals were kept in standard housing, with 12 h day/night cycle, and food and water provided *ad libitum*. Anaesthesia was induced with isoflurane 3.5% in 1:4 O₂ to air mix. Mice were endotracheally intubated, and positioned onto an animal MRI-compatible support, equipped with a hot water-flowing bed, and ear-bars to maintain the animal stable. Mice were ventilated mechanically with a small animal ventilator (CWE, Ardmore, USA) at 80 breaths per minute, with 1.8 ml/min flow. The tail vein was cannulated to administer anaesthetic and muscle relaxant. A bolus injection of medetomidine 0.05 mg/kg and pancuronium bromide 0.2 mg/kg was administered, and isoflurane was reduced to 1.5%. After 5 min, an infusion of medetomidine 0.1 mg/kg/h and pancuronium bromide 0.4 mg/kg/h was administered, and isoflurane was further reduced to 0.5%. The temperature was monitored using a rectal thermometer probe, and maintained at 36.5 ± 0.5 °C throughout measurement. Physiological parameters during anaesthesia were acquired in 5 mice outside the magnet using a mouse pulse oximeter placed on the left hind paw (MouseOX Plus, STARR Life Sciences). During physiological testing, pancuronium was omitted to allow testing of the reflex response to forelimb pinches.

Dataset description

Functional imaging data were acquired in three separate runs, and then grouped into different datasets for the analysis. Run 1: 14 female mice imaged at baseline (ME1 dataset). Run 2: 25 male mice imaged first at baseline, during which two fMRI scans separated by 30 min were acquired. The animals then underwent a chronic psychosocial stress (CPS, see below) paradigm and were imaged post-treatment. Data from this run were included in two datasets: ME2 consisting of only the baseline session and CPS2 including both baseline and post-treatment session. Run 3: 53 male mice imaged at baseline followed by CPS paradigm and imaged post-treatment. Data from this run, for which stationary FC analysis has been reported previously (Grandjean et al., 2016a), were divided into the FIX dataset consisting of only the baseline session and CPS1 dataset including baseline and post-CPS session. These datasets were further grouped as ME(all), encompassing datasets processed with multi-echo pipeline (ME1 and ME2), and CPS(all), encompassing all datasets from the CPS paradigm (CPS1 and CPS2). Datasets and respective acquisition procedures are detailed in Table 1.

Chronic psychosocial stress

Chronic psychosocial stress (CPS) was conducted as described previously (Azzinnari et al., 2014; Fuertig et al., 2016). Briefly, each C57BL/6 CPS mouse was placed singly in the home cage of an aggressive CD-1 mouse, separated by a transparent, perforated divider. Across 15 days, the CPS mouse was placed daily in the same compartment as the CD-1 mouse

Table 1
Datasets description.

Condition	Label	Run	Description	Sample	Parameters	XNAT project ID
Baseline	ME1	1	One fMRI scan measured in each animal.	N=14	C57BL/6 females ME-EPI TR=1.5 s, volumes=600 meica.py	ME_epi_mouse
	ME2	2	Two fMRI scans (S1 , S2) were measured 30 min apart in each animals (obtained as baseline scan of CSD2 dataset)	N _{S1} =25 N _{S2} =25	C57BL/6 males ME-EPI TR=1.5 s, volumes=360 meica.py	CSD_ME_MOUSE
	ME(all) FIX	3	ME1 and ME2 datasets combined One fMRI scan measured in each animal. (obtained as baseline scan of CPS1 dataset)	N=64 N=53	C57BL/6 males SE-EPI TR=1 s, volumes=360 FIX	CSD_MRI_MOUSE
CPS	CPS1	3	Animals were measured during a baseline session (FIX). Following that, animals were separated into Chronic Psychosocial Stress (CPS) and control (CON) groups. The CSD paradigm was applied during 15 days. Animals were measured in a post-session.	N _{CON} =27 N _{CPS} =26	C57BL/6 males SE-EPI TR=1 s, volumes=360 FIX	CSD_MRI_MOUSE
	CPS2	2	Animals were measured during a baseline session (ME2). Following that, animals were separated into Chronic Psychosocial Stress (CPS) and control (CON) groups. The CSD paradigm was applied during 15 days. Animals were measured in a post-session.	N _{CON} =12 N _{CPS} =9	C57BL/6 males ME-EPI TR=1.5 s, volumes=360 meica.py	CSD_ME_MOUSE
	CPS(all)		CPS1 and CPS2 datasets combined	N _{CON} =39 N _{CPS} =35		

for either a cumulative total of 60 s physical attack or 10 min maximum. To prevent bite wounds, the lower incisors of CD-1 mice were trimmed regularly. The CPS×CD-1 mouse pairings were rotated so that CPS mice were placed in the home cage and confronted with a novel CD-1 mouse each day. This CPS procedure was conducted for 15 days, between 14:00 and 16:00 h. Control mice remained in littermate pairs, the standard condition in our laboratory, and were handled and weighed daily. On day 16, post-treatment fMRI measurements were conducted (Grandjean et al., 2016). Group sizes for the two datasets (CPS1, CPS2, see previous section) are detailed in Table 1.

MRI acquisition

Images were acquired on a Biospec 94/30 small animal MRI system (Bruker BioSpin MRI, Ettlingen, Germany) equipped with a linear volume resonator coil for transmission and a 2×2 phased-array cryogenic surface receiver coil. Images were acquired using Paravision 6 software. Tripilot images were acquired to ensure proper positioning of the mice with respect to the coil and the magnet isocenter. Shim gradients were adjusted using a mapshim protocol, with an ellipsoid reference volume covering the whole cerebrum. Gradient-echo echo planar images (EPIs) were acquired either with multi-echo (me-) or single-echo (se-) EPI. Me-EPIs were acquired with repetition time TR=1500ms, echo time TE=11.5/17.3/23.1ms, flip angle FA=60°, matrix size MS=60×30, field of view FOV=18.2×9 mm², slice number NS=20, slice thickness ST=0.3 mm, slice gap SG=0.05 mm, acceleration factor AF=1.4, band width BW=250,000 Hz, and saturation slice covering the lower non-brain portion of the head. Se-EPIs were acquired with TR=1000 ms, TE=9.2 ms, FA=90°, MS=90×70, FOV=20×17.5 mm², NS=12, ST=0.5 mm, SG=0.2 mm, AF=1.2, and bandwidth BW=250,000 Hz.

Data processing

The datasets used in this study are publicly available on the central.xnat.org repository; the project ID for each dataset is provided in Table 1.

Multi-echo images were processed using meica.py script (AFNI, <http://afni.nimh.nih.gov/>). Briefly, the script performs de-spiking, motion correction and skull stripping, followed by an independent component analysis (ICA) decomposition of the images. For each component, the TE dependency of the signal time series is estimated. Components with a time series scaling with TE are considered BOLD-related, whereas components that do not scale with TE are considered non-BOLD, e.g. motion-, physiology- or scanner-related artifacts. The non-BOLD components are regressed out from the time series to provide a de-noised image. These were corrected for B1 field inhomogeneity and transformed to the AMBMC reference MRI template space (Australian Mouse Brain Mapping Consortium, <http://www.imaging.org.au/AMBMC>) using linear affine and non-linear greedy SyN transformation (ANTs V2.1, <http://picsl.upenn.edu/software/ants/>).

Single-echo images were processed as in Zerbi et al. (Zerbi et al., 2015) using FMRIB's ICA-based Xnoiseifier (FIX v1.062 beta, <http://fsl.fmrib.ox.ac.uk>) (Salimi-Khorshidi et al., 2014). Images were skull stripped and transformed to the AMBMC reference MRI template space as described above. Individual-level independent component analysis (ICA) was performed, and the resulting components were classified using a classifier from a previous study (Zerbi et al., 2015). The components classified as noise were regressed out from the time series.

Brain parcellation was based on a components atlas previously extracted in a group-level ICA containing 17 non-overlapping ROIs (Fig S2) (Zerbi et al., 2015) and further described in (Grandjean et al., 2016b). Dual regression (FSL 5.0.1, <http://fsl.fmrib.ox.ac.uk>) was performed to estimate the reproducibility of the components at the individual level.

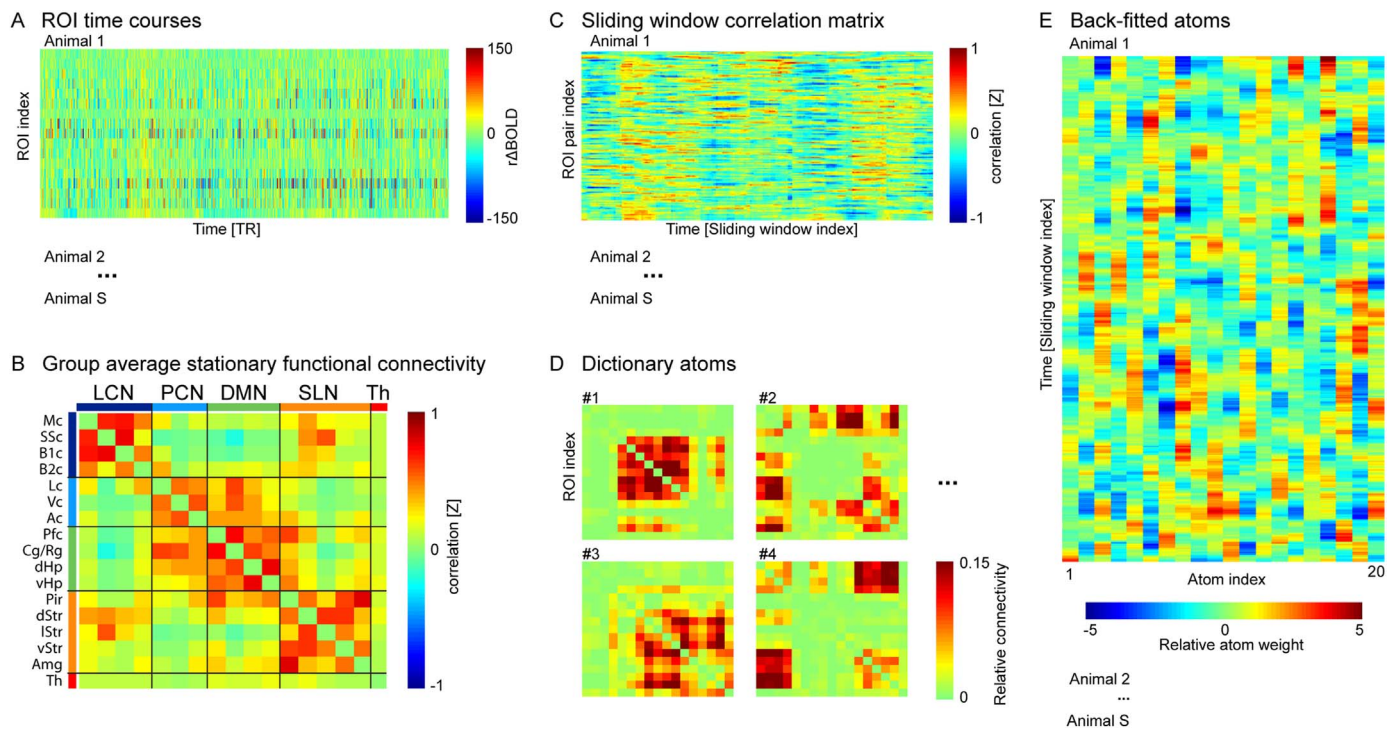


Fig. 1. Method summary. A) For each animal, the time series describing the activity of the atlas components were extracted. B) Full correlations between the time series were computed and averaged across ME(all) dataset (see Table 1) to obtain a stationary functional connectivity matrix. Functional connectivity presents a modular organization, split into a lateral cortical network (LCN), an associative cortical network (PCN), a default-mode network (DMN), a striatal-limbic network (SLN), and the thalamus (Th). C) The time series were analyzed with Pearson’s correlation coefficient within sliding windows. Sliding-window correlation matrices describing the degree of whole-brain regional interactions at each time point for each mouse are obtained. D) Through dictionary learning, building blocks of dynamic functional connectivity, the atoms, are extracted. The algorithm imposes that they be spatially sparse, non-negative, bounded, and that they occur sparsely over time. E) Separately for each mouse, sliding-window correlation matrices are approximated by an atom through univariate regression using least-square minimization, which generates an animal-specific weight time course for each atom. ROI abbreviations shown in (B) correspond to: motor (Mc), supplementary (SSc), barrel field 1 and 2 (B1c, B2c), limb (Lc), visual (Vc), auditory (Ac), prefrontal (Pfc), and cingulate/retrosplenial cortices (Cg/Rg), dorsal and ventral hippocampus (dHp, vHp), piriform cortex (Pir), dorsal, lateral, and ventral striatum (dStr, lStr, vStr), amygdala (Amg), and thalamus (Th).

Sliding window correlation

The regional time courses extracted from the brain parcellation were first high-pass filtered with a cut off frequency of 0.02 Hz (Fig. 1A) (Leonardi and Van De Ville, 2015). Dynamic functional connectivity between the filtered time series was computed with pairwise Pearson correlations using rectangular sliding windows of length 30 TRs corresponding to 45 s and step size 1 TR, in line with previous studies of similar temporal resolution (Hutchison et al., 2013; Leonardi et al., 2013; Sakoglu et al., 2010). Correlation values were z-transformed, and the connectivity matrices obtained for each time window were vectorized and stacked to yield a $K \times N$ matrix A_s for each subject s , with K the number of pair-wise connections and N the number of windows (Fig. 1C). To solely address the fluctuations of connectivity over time regardless of their mean level (which may differ across subjects), the matrix A_s was row-wise de-meaned (Leonardi et al., 2013). This changes the interpretation of the final derived dFC patterns, which will highlight in our case increases/decreases in connectivity with respect to the mean (stationary FC), rather than high/low connectivity values. To further investigate the effect of demeaning, the computation was repeated without this operation and the results were compared. The $S=64$ subject-specific matrices (ME(all) dataset, Table 1) were then concatenated into a data matrix $C^{K \times N \times S} = [A_1 | \dots | A_S] = [c_1 | \dots | c_{N \cdot S}]$, with $N \cdot S$ the product between the number of windows and the number of subjects.

Surrogate dataset generation

As sliding window correlation analysis has been shown to induce spurious correlations (Leonardi and Van De Ville, 2015; Lindquist et al., 2014), we performed a test for the presence of significant dFC in

the matrix C . We generated 1’000 surrogate sets of time courses for each resting-state scan of the ME(all) dataset using the amplitude-adjusted phase randomization procedure, similar to Betzel et al. (2016). This means generating surrogate time courses with randomized phase, but preserving a similar amplitude distribution, an approximately similar frequency spectrum, and a similar stationary connectivity pattern compared to the real data. Surrogate data underwent then sliding window correlation analysis, and subsequent temporal demeaning of pair-wise correlations as applied to the real time courses. For each scan, a distribution of dFC fluctuations around the mean was obtained, and its 2.5th and 97.5th percentiles were extracted as significance thresholds for dFC excursions.

Estimation of dynamic functional connectivity networks with dictionary learning

Dictionary learning was then applied to derive a set of signature connectivity patterns with strong explanatory capabilities, i.e. *atoms*. We generated a dictionary $D^{K \times M} = [d_1 | \dots | d_M]$, with $M=20$ K -dimensional column vectors as simple building blocks of whole-brain connectivity, the atoms, and a coefficient matrix $W^{M \times N \cdot S} = [w_1 | \dots | w_{N \cdot S}]$, with the columns containing coefficients describing how these atoms should be combined to generate a good approximation of the set of signals in C . Minimization of the cost function:

$$f(W, D) = \frac{1}{N \cdot S} \sum_{i=1}^{N \cdot S} \|w_i\|_1 \cdot t. \quad \|c_i - Dw_i\|_2^2 \leq \lambda$$

using a sparsity-enforcing algorithm yielded D and W . To prevent convergence to a set of atoms similar to the ones that would be retrieved by PCA (by definition, an optimal set in terms of explained variance to

linearly reconstruct the signal), λ was set to

$$\lambda_1 = 2 \cdot E_{PCA} = \frac{2}{N \cdot S} \sum_{i=1}^{N \cdot S} \|c_i - \tilde{c}_i\|_2^2$$

with \tilde{c}_i the signal frame approximation obtained by projection onto the space of the first M PCA components. A range of λ_1 values between $0.5 \cdot \lambda_1$ and $2 \cdot \lambda_1$ were tested, yielding qualitatively similar resulting atoms.

In order to retrieve easily interpretable atoms, we required them to be energy-bounded and positive by imposing the set of constraints

$$C \triangleq \{D \in \mathbb{R}^{K \times M} \text{ s. t. } \forall j = 1, \dots, M, \forall i = 1, \dots, K, \quad d_j^T d_j \leq 1, D_{ji} \geq 0\}$$

We performed dictionary learning 100 times (or *folds*; 400 iterations for the first fold, 200 for the subsequent ones). We matched the obtained atoms with the Hungarian algorithm (Kuhn, 2010), using spatial correlation as the similarity metric and the first fold as reference. To recover a robust final dictionary, we averaged, for each atom, the fold instances exhibiting similarity above the median value across all folds (Fig. 1D). Similarity was notably elevated in the case of most trials and the few outliers were not included in the averaging process. Animal-specific time-dependent contributions of atoms were obtained by back-projection of the dictionary onto the original dFC dataset using least-square fitting (Fig. 1E).

Generalization of dictionary learning estimation

To assess the reproducibility of the estimated atoms, 100 new sets of atoms were generated *de novo*, as described above for different window lengths or datasets. The newly generated atoms were compared to the reference atoms using spatial correlation as similarity metric, and using a nonparametric approach to define a similarity significance threshold. For each comparison (between reference and new dataset), we generated a null distribution of similarity values by including all within-dataset similarities across atoms. The 95th percentile (Bonferroni corrected for M tests performed) of this distribution was chosen as significance threshold. Then, we matched the atoms of the two datasets with the Hungarian algorithm and the resulting similarities across matched atoms were compared to the threshold.

Statistical analysis of group difference

Statistical analysis was performed in R 3.2.4 (The R Foundation for Statistical Computing, Vienna, Austria), using linear mixed models (lme4 package) for each atom separately. The absolute sum of time-dependent contributions of atoms relative to the number of sliding-window frames was used as a response variable. In the case of CPS analysis, session (baseline and post-treatment) and groups (CPS and control) were modelled as fixed effects, and the individual animal intercepts were modelled as random effects. Statistical comparisons were performed using contrast analysis (multcomp package), testing for a session X group interaction effect followed by post-hoc test (chronic stress effect in CPS group, or post-treatment vs baseline in the control group specifically). In the case of anaesthesia duration analysis, scan order (scan 1 and scan 2) was modelled as a fixed effect, and the individual animal intercepts were modelled as random effects. A contrast was designed to compare scan order. False discovery rate (FDR) was used to correct for multiple comparisons performed across atoms. To thoroughly assess whether observed group differences in dFC properties (upon modified anaesthesia level or psychosocial stress induction) were due to dynamic brain connectivity properties without methodological confounds, we employed a similar surrogate data generation strategy as that described above (see Surrogate dataset generation), except we modified the phase of each time course independently of the others for a full breakdown of connectivity properties. 1'000 such surrogate sets were generated for each resting-state scan (under the null hypothesis of a group difference not

generated by dFC), and statistical measures of group differences were extracted to build a null distribution, to which the real group difference values were compared. Significance was declared if the effects estimated with contrast analysis in the linear mixed model survived both FDR correction and were outside the 95th confidence interval estimated in the surrogate datasets, and are indicated as (**) in the figures. Significant effects estimated with contrast analysis that did not survive the FDR correction threshold, but were outside of the 95th confidence interval, are indicated as (*).

Results

Functional brain parcellation and quality control

Resting-state fMRI data sets acquired from anesthetized mice were of high quality, and presented minimal distortions even at higher TE (Fig S1A). The maximal relative displacement during acquisition was estimated at 0.023 ± 0.010 mm, corresponding to 7% and 10% of the voxel dimensions for multi-echo and single-echo EPI, respectively. Group average and standard deviation of the co-registered images indicated good overlap with the reference template, and a homogeneous standard deviation distribution (Fig S1B, ME(all) dataset). Time series were extracted according to a mouse brain parcellation derived from a prior group-level independent component analysis (ICA; Fig S2) (Zerbi et al., 2015). Similar components were reported in previous studies, including with different anaesthesia regimen, e.g. (Grandjean et al., 2014a; Sforazzini et al., 2014). Mouse resting-state networks are generally considered to be organized with a bilateral structure (Gozzi and Schwarz, 2016), we have thus decided to use the components as such rather than artificially separating ROI per hemisphere. Further, we have opted for a data-driven parcellation in order to retain relevant functional networks compared to anatomical-based atlases which may artificially split or merge these networks. Frequency analysis for time series extracted in the supplementary cortical component indicated a spread frequency distribution peaking near 0.15 Hz (Fig S3A, B, and C), comparable between datasets, and consistent with previously described distributions related to medetomidine in both mice and rats (Grandjean et al., 2014a; Kalthoff et al., 2011). In time series extracted prior to noise removal with either meica.py or FIX, peaks likely related to breathing artefacts were observed near 0.13 and 0.18 Hz in multi-echo datasets (Fig S3D and E) and near 0.33 Hz in the single-echo dataset (Fig S3F). These peaks were absent in the denoised dataset time series, indicating effective identification and removal of artefact in the fMRI time series. Dual regression was used to estimate individual-level maps of each of the components. Most cortical components and all striatal components displayed highly reproducible clusters, with 100% of the individual maps presenting β -estimates ≥ 15 , while the visual cortex, piriform cortex, dorsal and ventral hippocampus, and in the most pronounced manner, the thalamus, were embedded in more spatially disparate clusters across mouse subjects (Fig S4). Lower reproducibility of these latter components may be due to susceptibility artefacts in these regions, and in the case of the thalamus, anaesthesia effect related to medetomidine (Fukuda et al., 2013; Grandjean et al., 2014a; Nasrallah et al., 2014). Dual regression analysis carried on ME1, ME2 and FIX datasets did not reveal substantial differences related to data acquisition and processing (multi-echo vs. single-echo), and there were no significant gender or body weight effects in control animals. Group average stationary FC networks were reconstructed by computing Pearson correlations for all the pairs of time-series extracted from the ICA-based atlas (Fig. 1A and B, ME(all) dataset). This analysis revealed an organization of the components into distinct modules. A lateral cortical network (LCN) was found to include the motor, supplementary, and both barrel field cortical components similarly to previous reports (Liska et al., 2015; Zerbi et al., 2015). The posterior cortical network (PCN) included the limb, visual, and auditory cortex. The DMN was found to encompass the prefrontal and

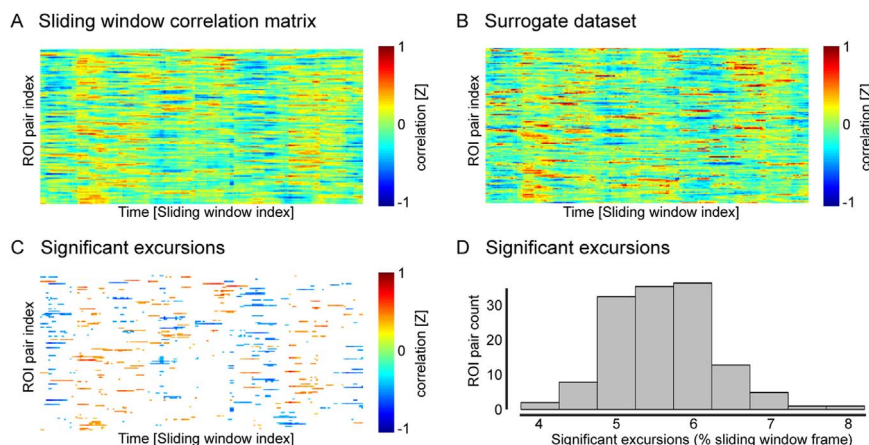


Fig. 2. Surrogate datasets and significant excursions. Surrogate datasets were generated to match the amplitude and frequency spectrum of original extracted time courses. The corresponding sliding window correlation matrices in a representative individual (A) and corresponding surrogate (B) present comparable features. Dynamical correlation fluctuations in the surrogate datasets were used to estimate 95th confidence interval for every individual and interactions between ROI pairs. Dynamical correlations outside the confidence intervals are indicated as significant excursions, shown for a representative individual (C). At the group level, these significant excursions were observed between all ROI pairs and corresponded to $5.6 \pm 0.6\%$ of the dynamic correlation fluctuations in the sliding window correlation matrices (D).

the cingulate/retrosplenial cortex as well as the dorsal and ventral hippocampal components. A striatal-limbic network (SLN) included dorsal, lateral, and ventral striatum, but also the amygdala and piriform cortex. Again, the thalamus stood out, as it displayed minimal correlation to any other component in the stationary FC map. Overall, the different quality assurance steps indicate that the datasets used in this study fulfil stringent quality standards, which is a prerequisite for dFC analysis.

Dynamic functional connectivity states reveal distinct structured organization

Sliding-window correlation analysis with window length corresponding to 45 s (30 TRs) was applied to the time-series of naïve mice between every pair of components in order to estimate the temporal variation in correlation strength (Fig. 1C, ME(all) dataset). dFC matrices obtained for each mouse were Fisher r -to- z transformed and centred across the scanning session. Surrogates to the ME(all) datasets were generated to match amplitude and frequency spectra of the real data. The sliding window correlation matrices in the surrogates presented similar features as in the real data (Fig. 2A and B). The test of FC non-stationarity yielded $5.6 \pm 0.6\%$ significant excursions between ROI pairs at the group level (Fig. 2C and D), well within the range of the previously reported 6.8% in human datasets (Betz et al., 2016).

Atoms, i.e. elementary building blocks of whole-brain dynamic connectivity representing specific dFS, were estimated from the population data using dictionary learning. Different dictionary sizes were tested, $M=[10, 15, 20, 25, 30]$, and found to explain 41, 51, 58, 64, 69% of the variance when regressed back into the individual sliding window correlation matrices. The final set of atoms were estimated with $M=20$ as it explained $\sim 60\%$ of the dFC variance in ME(all) dataset. The individual atoms exhibited a high degree of structure (Fig. 3, Fig S5), in particular, many of the atoms revealed dominant between-module and within-module interactions. For example, dFS #1 highlighted between- and within-module interactions encompassing the PCN and DMN, dFS #3 an interaction between the LCN and SLN, and dFS #5 between the LCN and PCN. Other dFS reflect predominant within-module interactions such as dFS #10 and #12, revealing interactions within the SLN and LCN, respectively. Interestingly, among the dFS we did not observe connectivity patterns involving the thalamus, with the exception of dFS #16 which showed strong interaction between the thalamus and the other modules. We conclude that dFC analysis reveals distinct dFS, the structure of which reflects

dominant within- and between-module interactions. This way, signal variability over time is taken into account to provide a more complete picture of brain activity.

Reproducibility of the atoms across parameters and data sets

Atoms are reproducible across a range of window length

To investigate the stability of the atoms across a range of different parameters, we performed the same dictionary learning process using varying window lengths corresponding to 15 s, 30 s, 45 s, 60 s, 75 s, 90 s, 105 s, 120 s, 135 s, and 150 s for the sliding-window correlation (ME(all) dataset). For each window length, high pass filter was adapted ranging from 0.0667 to 0.0067 Hz, corresponding to $1/\text{window length}$ as the cutoff (Leonardi and Van De Ville, 2015). The 100 newly estimated sets of 20 atoms were compared to the reference atoms estimated with window length corresponding to 45 s using a similarity index (Fig S5). Similarity indices for matched atoms across datasets were compared to a null distribution generated from the similarities estimated on within-dataset non-matched atoms. Indices above the 95th percentile threshold in the null distribution were considered significant. The odds ratio denotes how many times more likely it is that the similarity between matched atoms is significant compared to chance level, i.e. 5%. For instance, for window length corresponding to 45 s, 16 out of 20 atoms presented odd ratios greater than 10, indicating that the similarity for a given pair resulted in significance in more than 50% of the cases, that is 10 times more significant than chance. From this comparison, the patterns elucidated by dictionary learning appear consistent across a wide range of window lengths. Only for extreme window lengths (i.e. 15 s and 150 s) did we obtain noticeably reduced similarity indices (Fig. 4A), consistent with the notion that long window lengths result in lower sensitivity to the dynamic features of the signal while too short ones may induce spurious fluctuations (Leonardi and Van De Ville, 2015).

Dictionary atoms are reproduced in different datasets

To investigate if the derived atom patterns could be generalized, we applied the dFC analysis to the FIX dataset ($N=53$), which had not been used for the estimation of the reference set of dFC, and which is based on FMRI's ICA-based Xnoiseifier (FIX) for artefact removal (Salimi-Khorshidi et al., 2014; Zerbi et al., 2015). Additionally, we estimated atoms in sub-sets of the ME(all) dataset, i.e. ME1 ($N=14$), ME2(1) ($N=25$), and ME2(2) ($N=25$), to test for the generalisation of the atom patterns within ME(all), in particular as these sub-sets differ in gender, acquisition duration, and anaesthesia duration. In all

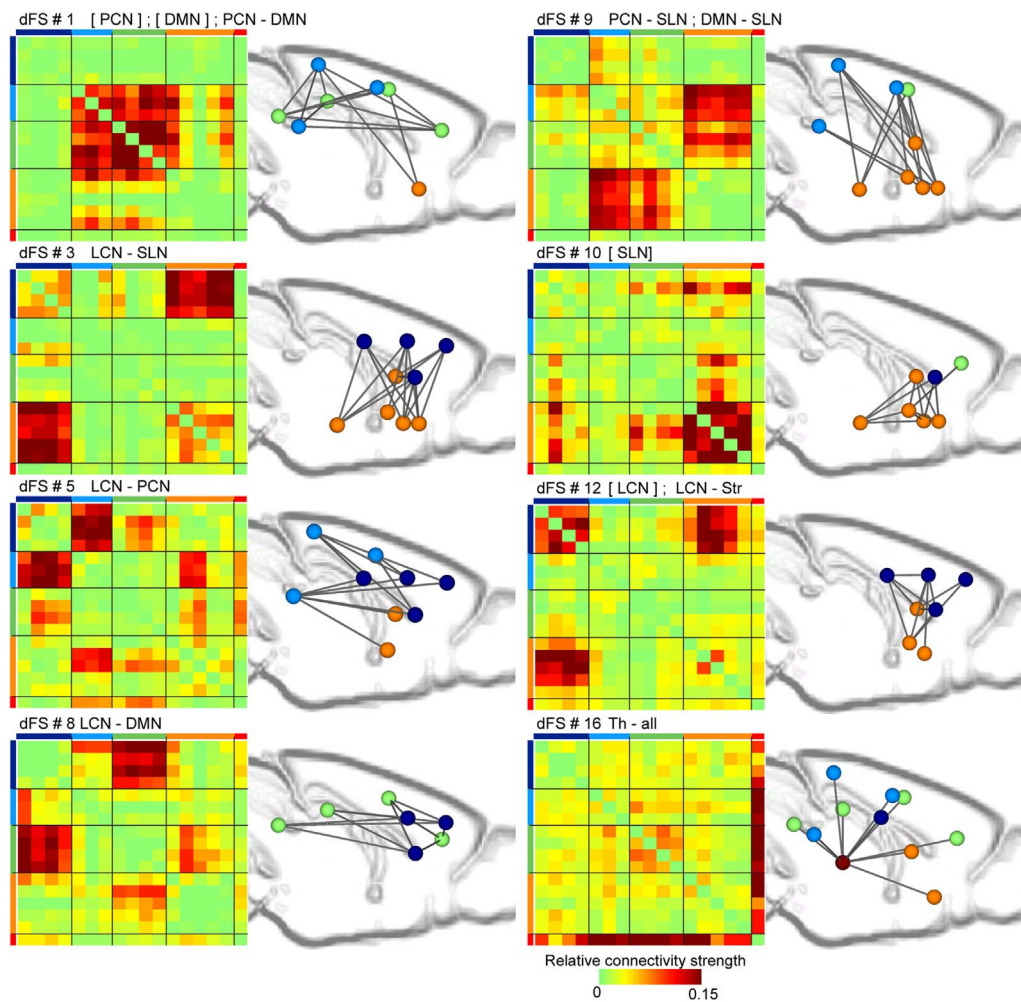


Fig. 3. Selected dynamical functional states. Atoms resulting from the dictionary learning algorithm present a high degree of structure in the dynamical functional states (dFS), with several states organized into dominant between- or within-module interactions. dFS #1 presents dominant connectivity strength within the PCN and within the DMN, as well as interactions between the PCN and DMN. dFS #3, 5 and 8 indicate dominant interactions between the LCN and, respectively, the SLN, PCN, and DMN. dFS #9 shows interactions between the SLN and the PCN and DMN, whereas dFS #10 displays interactions within the SLN. dFS #12 illustrates interactions within the LCN, and between the LCN and striatum. dFS #16 denotes interactions between the thalamus and each other region. In both matrix and ‘ball and stick’ representations, modules are color-coded as: LCN = dark blue, PCN = light blue, DMN=green, SLN=orange, thalamus=red. The ball and stick representation shows edges with connectivity strength ≥ 0.15 , overlaid on sagittal mouse brain delineations. ROI indices are provided in Fig. 1B and further detailed in Fig. S2.

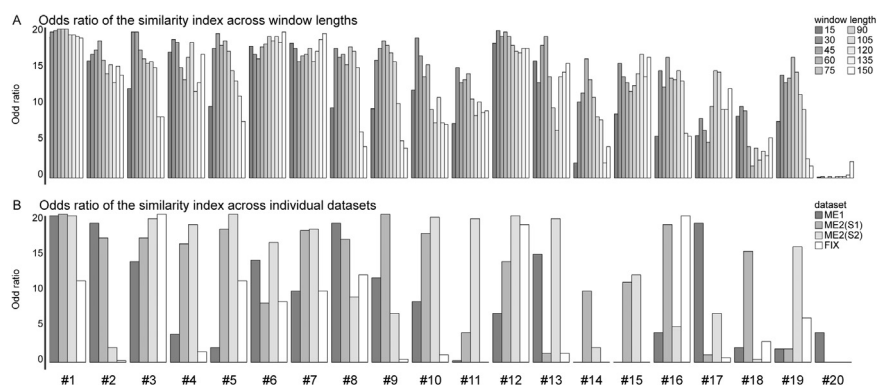


Fig. 4. Reproducibility of the atoms across different window lengths and datasets. A) Sliding window correlations were estimated using window length 15 s, 30 s, 45 s, 60 s, 75 s, 90 s, 105 s, 120 s, 135 s, and 150 s (corresponding to 10, 20, 30, 40, 50, 60, 70, 80, 90, and 100 TRs). Atoms were estimated with dictionary learning and compared to the reference atoms in Fig. S4 with similarity index. The odds ratio indicates how many times more likely it is for the similarity outcome to be real rather than random. High odds ratios (> 10) are observed for 19/20 atoms, and large range of window length (except for atoms #10, 11, 18, 20), denoting comparable features in these atoms to the reference set of atoms. B) Atoms were estimated using different datasets: ME1 ($n=14$, volumes=600), scans 1 and 2 from ME2 ($n=25$ each, volumes=360), and FIX ($n=53$, volumes 360) using window length corresponding to 45 s. Reproducibility of the atoms in individual datasets varied for each atom and dataset. High odds ratios were observed for atoms #1, #2, #3, and #8 in ME1 dataset. Atoms #4, #7, #10, and #12 were recovered in both ME2 scans 1 and 2 with significant similarity to the reference atoms. Data from the FIX dataset were not used to estimate the reference atoms, but nevertheless, significant similarity to the reference set was observed for atoms #1, #3, #5, #6, #7, #8, #12, and #16.

datasets, the reference atoms displaying a high degree of structure, such as dFS #1, #3, #6, #7, #8, #9, #12 and #16, exhibited significant similarity across datasets and an odds ratio above 5 (Fig. 4B), whereas atoms containing fewer indication of structure, such as #11, #13, #15 and #20, were less reproducible in individual datasets. Several atoms were highly reproduced in individual datasets but not in others, for instance atom #2 presents low odd ratios in both ME2(S2) and FIX datasets but high odd ratios in ME1 and ME2(S1). These observations are consistent with the notion that some of the atoms estimated with dictionary learning may be generalized, even following a different preprocessing pipeline, whereas others may represent states occurring less frequently or may actually constitute confounding noise contributions. Notably, the individual datasets used in the latter analysis contained fewer sliding-window correlation frames available to the dictionary learning algorithm compared to ME(all), a factor which may explain the presence of less reproducible atoms. Finally, we estimated atoms in ME(all) using 45 s window length but omitting the demeaning of the sliding window correlation matrix. Newly estimated atom sets did not present any significant similarity to the reference set. Indeed, atoms generated in the absence of de-meaning (Fig S6) presented patterns comparable to the stationary FC matrix (Fig. 1B). To explain this, we estimated the average power across subjects of the stationary FC E_{stat} (that we remove in the demeaning) and compare it to the average power of the demeaned and non-demeaned dFC (E_{dyn} and $E_{stat+dyn}$ respectively). In our data, $E_{stat}=16.79$, $E_{dyn}=6.14$ and $E_{stat+dyn}=22.93$, verifying therefore the following equations:

$$E_{stat+dyn} \geq E_{stat} + E_{dyn}$$

$$E_{stat} \gg E_{dyn}$$

These results highlight the predominance of the stationary FC on top of the dFC changes, and therefore explain why de-meaning is important to highlight the dFC patterns, otherwise covered by the stationary FC.

We conclude that the majority dFS yields a high degree of consistency across datasets acquired with different sets of animals or using different experimental parameters, as well as in the face of changes in parameters used in the analysis procedure.

Dynamic functional states are sensitive indicators of physiological and pathological states

Chronic psychosocial stress alters cortico-limbic dynamic functional state

Given the high degree of reproducibility of the estimated atoms, we examined whether these readouts could be used as sensitive indicators of alterations in physiological or pathological conditions. The CPS model comprises social stress leading to depression-relevant behaviours including increased fatigue and aversion to negative stimuli, and reduced interest in positive stimuli (Azzinnari et al., 2014). Two datasets were acquired (CPS1, CPS2; Table 1): Both datasets included a baseline fMRI scan, followed by the CPS or control paradigm, and a post-treatment fMRI scan. The CPS paradigm was associated with an increase in stationary FC within the cortical networks including the supplementary cortical component and DMN, as well as an increased connectivity between the amygdala and the DMN (Grandjean et al., 2016a). Sliding-window correlation analysis was performed with window length 45 s (corresponding to 30TRs for me-EPI datasets and 45TRs for se-EPI). The reference atoms resulting from dictionary learning estimated in healthy control animals (Fig S5) were back-fitted using least-square regression onto the original dFC matrices to obtain time-dependent weights of each atom in each individual (Fig. 1E). This approach is comparable to the dual-regression framework where group-level components estimated in healthy controls individuals are used as reference to estimate individual-level networks, as applied previously to estimate stationary FC changes in CPS mice (Grandjean

et al., 2016a). Indeed, the approach assumed in this analysis is not to test for the presence of different atoms in the CPS groups, but to put in evidence differences in the atom fluctuations between CPS and control individuals. In order to test if the reference atoms estimated in control animals contributed equally in control and CPS individuals, explained variance was estimated in the CPS1 dataset which was not used to estimate the reference atoms. During the baseline session, the mean (± 1 standard deviation) explained variance was 48.2 ± 5.8 and 45.1 ± 5.7 for control and CPS groups, and 48.6 ± 6.4 and 47.7 ± 6.5 during the post-treatment session. Explained variance was lower than that in ME(all), which is to be expected as the latter was used to estimate the reference atoms. No significant session X group interaction or CPS effect could be put in evidence using a linear mixed model analysis, suggesting that the reference atoms explained similar portions of the sliding-window correlation matrices in all groups.

The absolute sum of the time-dependent weights relative to the number sliding-window frames for each atom was used as a response variable in linear mixed-model statistical analyses, one per atom, with contrasts to test for the interaction between group and session and CPS effect (post- vs. baseline in the CPS group specifically). The analysis was carried on CPS(all) dataset, which include scans acquired with se- (CPS1) and me-EPI (CPS2), yielding differences in sequence parameters, preprocessing pipeline, SNR, acquisition length, among other. In order to compensate for this, a balanced linear mixed model approach was used, with each individual including both a baseline and post-treatment session. Individual intercepts were added as random effects in the model in order to account for individual variability including the differences in these parameters in the statistical analysis. Significant interaction effects were found for dFS #2, surviving both FDR correction and comparison to the surrogate-based null distribution, and to a lesser extend dFS #11 and #16, which did not survive strict FDR correction, but were outside the 95th confidence interval defined using surrogate datasets. In all three instances, the interaction effect was confirmed to reflect a CPS group-specific effect in a post-hoc analysis (Fig. 5A). The atoms showing significant differences revealed an increased interaction effect between the LCN and the limbic areas (hippocampus, piriform cortex, and amygdala; dFS #2), and between the DMN and both LCN and SLN (cingulate/retrosplenial cortex and dorsal hippocampus to LCN and SLN; dFS #11), while the interaction between the thalamus and the other regions (dFS #16) appeared to be reduced (Fig. 5B). Statistics carried separately in individual datasets, CPS1 and CPS2 (Fig S7A and B), indicate the presence of similar effects in both datasets as described above. There was no comparable effect in the control group of any of the dFS shown to present a chronic stress effect (Fig S7C). Together, these underline the robustness of the effect induced by CPS on dFC patterns in the murine brain.

Anaesthesia duration alters both stationary and dynamic functional connectivity

The duration of anesthesia is a confounding element in rodent functional imaging studies; for example, Magnuson et al. (2014) found that long exposure to isoflurane compared to shorter exposure led to lasting altered connectivity patterns when anaesthesia was switched to medetomidine during fMRI recordings. We were therefore interested in studying the effects of prolonged anesthesia on stationary and dynamic FC. We compared two datasets obtained with the same mice under medetomidine/isoflurane anesthesia, one obtained 30 min after the other (ME2(S1), ME2(S2); Table 1). Physiological parameters recorded in a separate animal cohort indicated an increase in heart rate (336.8 ± 62.1 vs. 534.4 ± 157.0 beats per minute) and a corresponding decrease in pulse distension (21.8 ± 2.8 vs. 16.5 ± 6.1 μm) for time points corresponding to the second fMRI acquisition (55 to 60 min after medetomidine infusion onset) compared to the first (20 to 25 min after medetomidine infusion onset). At both time points, mice responded to mild pinches to the fore limb but presented no spontaneous motion. O_2 saturation was comparable at both times (99.0 ± 1.1 vs. $99.3 \pm 0.2\%$). Physiological parameters denote a brachy-

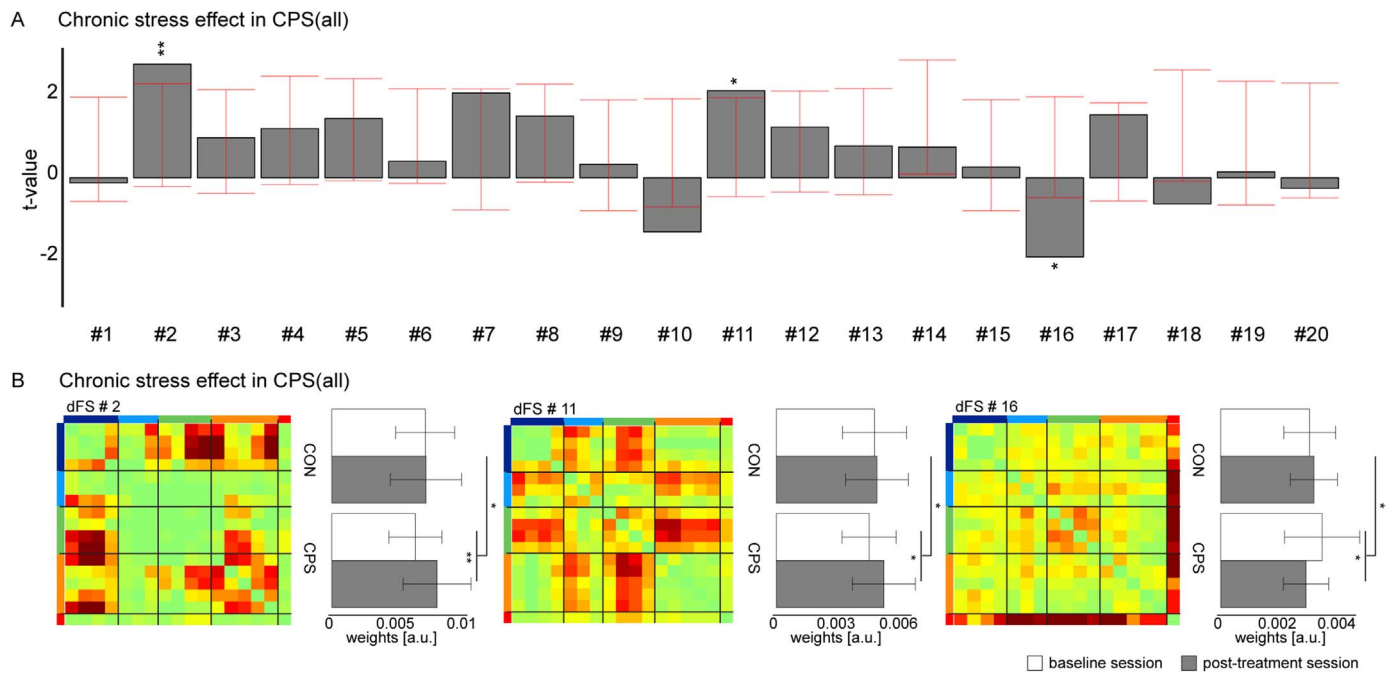


Fig. 5. Dynamic functional states are affected by chronic psychosocial stress. A) Chronic psychosocial stress leads to a significant increase in dFS fluctuations in several atoms in the CPS group post-treatment session compared to baseline, specifically in dFS #2, #11 and #16. Error bars indicate the 95th confidence interval for statistics estimated in surrogate datasets. B) The CPS group presents increased fluctuations compared to control and baseline in dFS #2 which describes interactions between the LCN and limbic-associated regions, the hippocampus, the amygdala, and the piriform cortex, and #11 which describes interactions between DMN (cingulate/retrosplenial cortex and hippocampus) and both the LCN and SLN. There was an opposite effect in atom #16, which describes interactions between the thalamus and all other regions in the atlas. Bar plots show mean absolute sum of dFS fluctuations ± 1 SD. * $p \leq 0.05$, ** $p \leq 0.05$ (FDR).

cardia effect induced by medetomidine for time points corresponding to the first scan as previously reported (Grandjean et al., 2014a) and a corresponding return to rates similar to those in isoflurane anaesthetised mice for the second time points, indicating a wash-out of the initial medetomidine bolus over time. Dual regression analysis revealed an increase in stationary FC in the second scan in the components barrel field 1 and 2, limb, visual and cingulate/retrosplenial cortices, and ventral hippocampus (Fig. 6A), while there was an opposite effect for the dorsal and lateral striata. The bidirectional nature of the changes is unlikely to be due to systemic cardiovascular changes only, indeed systemic physiological changes have been reported to lead to unidirectional BOLD changes (Schroeter et al., 2014). In fact, these changes are consistent with reduced medetomidine effect combined with isoflurane cumulative effects over time. Indeed, longer exposure to isoflurane has been reported to induce lasting FC (Magnuson et al., 2014). Isoflurane has been reported to reduce FC in the striatum, while medetomidine reduces cortical FC in a dose-dependent fashion (Grandjean et al., 2014a; Nasrallah et al., 2014). Despite the presence of the effects described above, atoms estimated with dictionary learning could be reproduced in both scans (Fig. 4B). The reference atoms resulting from dictionary learning (Fig S5) were back-fitted using least-square regression onto the original dFC matrices estimated with window length of 45 s (30TRs). Mixed model analysis comparing scans 1 and 2 revealed significantly increased atom fluctuations for dFS #3, #8, and #15 that were also above or below the 95th confidence interval estimated in surrogate datasets (Fig. 6B). The dFS found to exhibit the strongest anaesthesia effects were associated with the LCN and DMN dynamic interaction (dFS #8), and LCN and PCN with the SLN (dFS #15) (Fig. 6C). Dynamic interactions involving LCN and SLN (dFS #3) also presented a significant anaesthesia effect found with both mixed-model analysis and comparison to the null distribution estimated with surrogate dataset, however the latter did not survive FDR correction. We conclude that dFS display distinct responses to alterations in brain states induced by psychological and physiological factors.

Discussion

Studies of FC in humans and experimental animal models have shed light on the network topology of the healthy and diseased brain at a macroscopic level, revealing important information on the interplay between brain regions. Increasing evidence indicates that the assumption of a stationary connectivity network, inherent in the majority of the studies published to date, represents an oversimplified view of brain organization. Rather, functional networks have been proposed to be dynamic (Calhoun et al., 2014), i.e. the strength of connectivity between various brain regions is proposed to change over time and these changes are considered to be biologically meaningful. In contrast to conventional stationary FC analysis, dFC approaches allow for the exploration of dynamic aspects of brain network interactions. Despite the great potential of dFC as demonstrated in studies involving humans, the basis of this dynamic organization remains poorly understood. Animal studies should help in relating intrinsic FC fluctuations to other readouts of activity as well as in understanding the significance of dFC states induced by etiological factors of importance in brain disorders or pharmacological interventions. For the first time, we have investigated dynamic properties of FC in the mouse brain by applying dictionary learning to establish interpretable dFS. The combination of dietary animal handling to optimize physiological stability, high magnetic field strength and cryogenic receiver coil to increase signal-to-noise ratio, and use of an fMRI acquisition sequence that enhances the sensitivity to the blood oxygenation level dependent contrast, enabled us to record mouse brain datasets of a quality appropriate for valid dFC analysis.

The major finding of the study is the identification of reproducible dFS of the mouse brain exhibiting remarkable structure. The dominant dFS reflect interactions between and within network modules such as the default-mode, lateral cortical, posterior cortical and striatal-limbic networks. Previous dFC studies in humans, monkeys and rats did not capture such dynamics, possibly due to the complexity of the functional

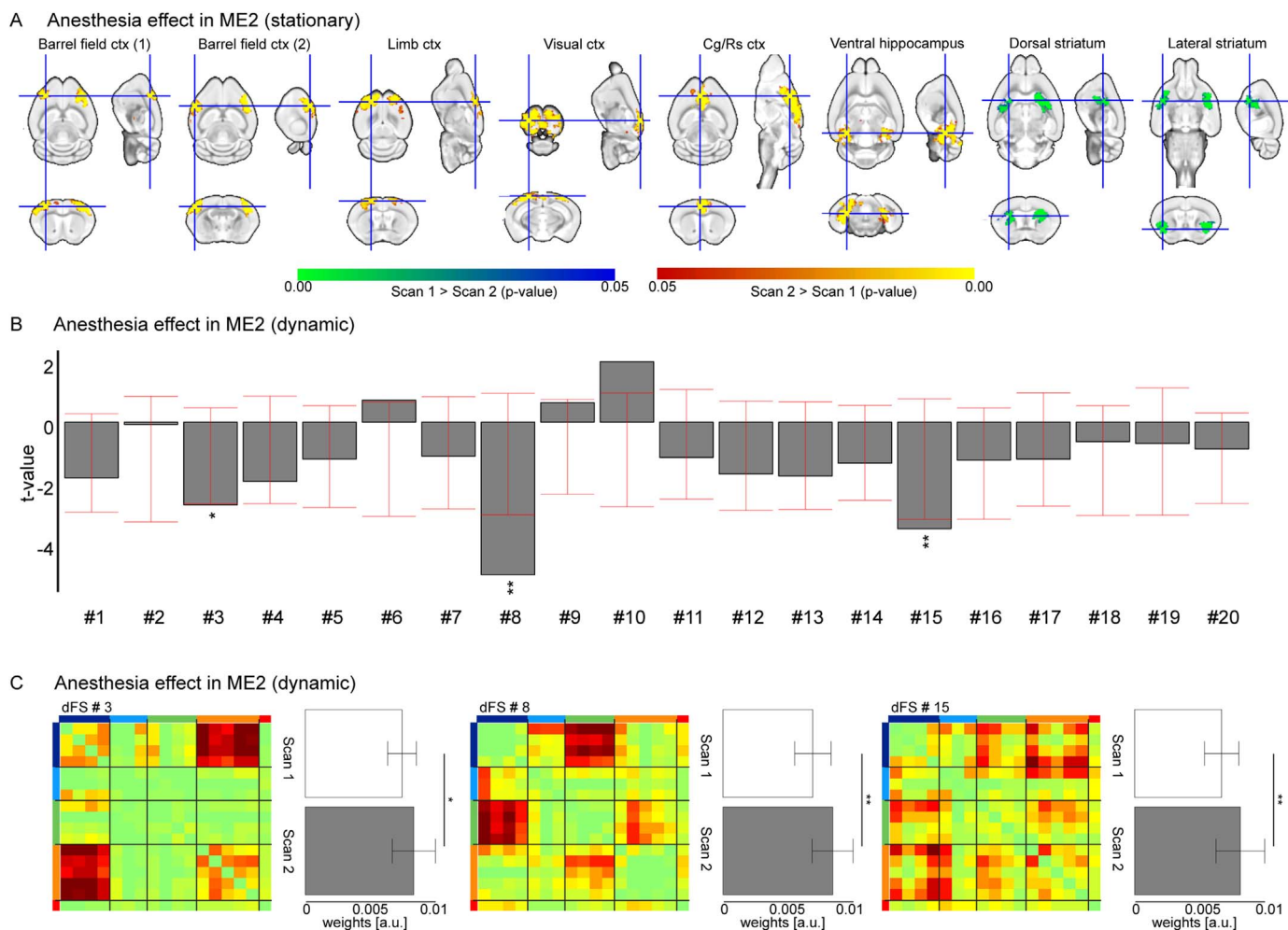


Fig. 6. Dynamic functional states are affected by anesthesia duration. A) Comparison of the stationary functional connectivity with dual regression of ME2(S1) and ME2(S2), acquired 30 min apart, highlights significant differences between the two scans. Cortical functional connectivity in the barrel field, limb, visual, and cingulate/retrosplenial cortices, as well as functional connectivity in the ventral hippocampus was increased in scan 2 compared to 1. The opposite effect was found in the dorsal and lateral striata, denoting a decrease in FC in scan 2 relative to 1 in each case. The color bar indicates the p-value. B) Significant changes in dFS fluctuations between the two scans were observed in several atoms and with different window lengths, namely dFS #3, #8 and #15. Error bars indicate the 95th confidence interval for statistics estimated in surrogate datasets. C) Anaesthesia effects are detailed for 3 dFS. These describe interactions within the DMN and between the LCN and SLN (dFS #3), LCN and DMN (dFS #8), and LCN and SLN (dFS #15). Bar plots show mean absolute sum of dFS fluctuations \pm 1 SD. * $p \leq 0.05$, ** $p \leq 0.05$ (FDR).

organization in primates and the methodological approaches applied to study dFC. In several reports, dFC analysis focused on a subset of brain regions such as the DMN (Chang and Glover, 2010), the oculomotor network (Hutchison et al., 2013), the motor cortex and caudate putamen (Keilholz et al., 2013), or the somatosensory cortex (Thompson et al., 2013). Other studies in humans employed a whole-brain approach (Allen et al., 2014; Chen et al., 2016; Leonardi et al., 2013; Liu and Duyn, 2013). In particular, Leonardi et al. introduced a PCA-based method to decompose whole-brain connectivity patterns into a set of orthogonal components termed eigenconnectivities (Leonardi et al., 2013). Allen et al. made use of an ICA-based brain parcellation followed by temporal clustering into a limited subset of connectivity states (Allen et al., 2014). Although both approaches could extract meaningful connectivity patterns, their interpretation remained difficult due to the contributions of numerous region-to-region relationships. More importantly, the dFC patterns did not reveal distinct interactions between modules of the stationary functional network. The refinement of previous analytical strategies through the addition of a dictionary-learning step enabled us to unravel the presence of structured dynamic interactions among modules of the stationary functional network organization of the mouse brain.

The use of sliding window correlations remains a matter of debate. Firstly, difficulties in reliably estimating individual-level dFC with

sliding windows were reported; however, these limitations could be offset by longer acquisitions or session and subject averaging (Hindriks et al., 2016). By concatenating sliding window correlation matrices from healthy control individuals, we obtained robust estimates of group-level atoms. These atoms were also extracted from smaller datasets, yet were found to be less robust, consistent with the notion mentioned above. Secondly, the selection of window length parameters remains an essential aspect of dFC analyses, as too small window lengths have been shown to induce spurious correlations (Leonardi and Van De Ville, 2015; Lindquist et al., 2014; Shakil et al., 2016). We have observed that the window length did not noticeably influence the estimation of atoms in this dataset as long as extreme values were avoided. Furthermore, we have generated surrogate datasets, and could confirm the presence of significant dynamic excursions in our datasets comparable to previous reports (Betz et al., 2016). Finally, surrogate time series was also used to estimate confidence intervals in our statistical comparisons, indicating that the presence of the effect in our real datasets cannot be directly related to artefacts induced by the sliding window correlation process.

Atoms established with dictionary learning in this study were found in an independent dataset, supporting the notion these dFS could be generalized to other mouse fMRI datasets. A few limitations need to be considered. Firstly, datasets were acquired with high SNR dataset, se-

EPI acquired with this protocol were reported to yield SNR ~ 170 (Zerbi et al., 2015), and while me-EPI yielded lower SNR for each individual echo, the effective SNR is expected to be increased when the individual echo images are combined. Other datasets may not yield comparably high SNR, which may impair the detection of such dynamic events. The minimal SNR requirements for optimal dFC detection remain a moot point to be addressed. Secondly, not all atoms could be recovered equally in all datasets. It is likely that some dFS are less frequent than others, or that they capture noise patterns, as supported by our results. Contrary to stationary FC, where methods exist to identify nuisance components based either on feature recognition using FIX (Salimi-Khorshidi et al., 2014; Zerbi et al., 2015) or physical properties of the BOLD signal using me-EPI (Kundu et al., 2012), methods to rationalize ‘signal’ from ‘noise’ dFS remain lacking. Similarly, the optimal number of atoms to include in the analysis remains a point to be addressed, as too few or too many atoms may lead to under- or over-fitting issues. In the present study, 60% of the variance explained was used as a heuristic-based choice leading to the identification of 20 reference atoms. In light of the above, all atoms were included in the analysis in order to avoid user selection bias. Finally, analyses were carried using reference atom estimated in healthy control. A study carried in human with post-traumatic stress disorder found that the patient group presented specific dFS (Li et al., 2014), it is thus plausible that the CPS paradigm causes not only changes in the reference atom fluctuation as reported in this study, but also in the atom structure. As mentioned above, robust atom estimation relies on the number of time frames available, which was insufficient in the CPS groups to carry the latter analysis. However, it should be noted that the reference atoms explained comparable variance in both control and CPS individuals, supporting the notion that changes in atom fluctuation rather than atom structure may explain changes taking place in the CPS model.

The biological relevance of these dynamic states is supported by the alterations observed in a model of social stress-induced depression-like brain and behaviour. CPS was associated with increased fluctuations in dFS involving interactions between the LCN and limbic regions: the prefrontal cortex, hippocampus, the piriform cortex, and the amygdala. In human major depression, increased dynamic interactions have been reported between the prefrontal cortex and the insula when comparing unmedicated patients with controls, an observation that has been linked to increased self-referential information processing and rumination (Kaiser et al., 2016). This may relate directly to our observation, as the insula overlaps with the supplementary cortical component in the mouse, a central structure of the LCN. While the human study focused on highlighting network fluctuations involving the prefrontal cortex (Sheline et al., 2010), the use of dictionary learning in our study enabled the identification of reoccurring states across the whole brain. Thus, we found increased fluctuations in dFS linking the LCN to the SLN and DMN in CPS mice, while interactions between the thalamus and all other elements of the ICA-based atlas were reduced in CPS mice, specifically. This may indicate increased cortico-cortical interactions between sensory-motor and higher-level networks such as the DMN, when thalamo-cortical interactions are decreased, consistent with the notion of dFC changes promoting the increased self-referential processes that occur in human depression (Manoliu et al., 2013; Sheline et al., 2010). Our dFC findings yield new insights into functional alterations induced by chronic social stress, relevant to human depression and complementing conventional stationary FC analysis (Grandjean et al., 2016a).

Anesthesia is a major factor affecting neural processing and thus functional networks and their interactions. A previous study in rat identified a notable effect of anesthesia duration on FC (Magnuson et al., 2014). We found that changes in the anesthesia duration had little effect on the qualitative nature of detected dFS, although there were quantitative effects on fluctuation amplitudes. The strongest anesthesia-duration effects on dFS involved the DMN, consistent with the importance of this network in controlling cognition, information

integration and wakefulness (Boly et al., 2012). Our results, in line with earlier reports from primates and rats (Barttfeld et al., 2015; Hutchison et al., 2013; Thompson et al., 2013), illustrate that aspects of dFC are retained in the anesthetized state. Nevertheless, dFC analysis appears sensitive to mild changes in anesthesia levels.

Dynamic analysis is a highly attractive measure as the organization of the dFS may actually reflect a composite aspect of neuronal computation. In fact, while, in mice, stationary FC reveals mostly homotopic coupling between brain functional units, dFC analysis suggests a potential wealth of functional interactions among these regions. The dFC between entire modules, e.g. LCN and DMN, may reflect the sharing of information from sensory integration in the LCN to higher-order associative processing within the DMN. Hence, the temporal interplay of dFS may enable episodes of segregation and integration between modules to support neuronal processing of information (Friston, 2002). The important question in this context refers to the link between neuronal events occurring at a millisecond timescale and episodes of dFS activation detected by fMRI, which span several seconds. Compared to electrophysiological measurements, current studies of dFC with resting-state fMRI are inherently limited to this slow time-scale due to the low-pass filtering effect of the hemodynamic response, as well as additional low-pass filtering introduced by sliding-window correlations (Leonardi and Van De Ville, 2015). As a consequence, linking neuronal events to dFS remains a major challenge. A first approach towards understanding this interplay combined invasive local electrophysiological recordings in the rat sensory cortex with fMRI, which indicated a correlation between sliding-window correlation in the slow frequency bands in the electrophysiological signal and in the fMRI signal (Thompson et al., 2013). Similarly, in human studies, scalp electroencephalogram topographies have been correlated with fMRI resting state networks (Britz et al., 2010). Studies linking direct readouts of neuronal activity to hemodynamic responses will be critical in order to relate dFS to neuronal events across the different time scales.

In conclusion, using stationary FC analysis in the mouse brain, we could identify five distinct modules from resting-state mouse fMRI data sets. Combining sliding-window correlation measurements with dictionary learning into a novel refined dFC framework, revealed consistent interaction patterns driven by fluctuations of connectivity, i.e. the occurrence of transient dFS that showed between- and within-module interactions. The structured dFS states were found to be remarkably robust against variations in experimental conditions and in processing parameters. Similarly, changes in brain state caused by psychosocial stress or altered physiology did not affect the nature of the dFS, but rather the coupling strength between the modules in a biologically meaningful manner. Analyzing dynamic aspects of functional networks at a whole-brain level significantly enhances our capabilities of studying the complex interplay of brain regions in information processing. Future studies in mice using either combined activity readouts or strategies to modulate network interactions are expected to shed light into the nature of this phenomenon, and to elucidate new biomarkers for brain disorders.

Acknowledgments

This work was supported in part by the Swiss National Science Foundation (grant number 310030_141202 and 310030_160310 MR; 205321_163376 to DVDV), the Swiss Foundation for Excellence and Talent in Biomedical Research (to CRP and MR), the Bertarelli Foundation (to TB and DVDV) and the Center for Biomedical Imaging (CIBM; to MGP). We thank Valerio Zerbi for critical reading of the manuscript and Prof. Thomas Yeo for providing the resources for the manuscript revisions.

Appendix A. Supporting information

Supplementary data associated with this article can be found in the online version at doi:10.1016/j.neuroimage.2017.03.026.

References

- Allen, E.A., Damaraju, E., Plis, S.M., Erhardt, E.B., Eichele, T., Calhoun, V.D., 2014. Tracking whole-brain connectivity dynamics in the resting state. *Cereb. Cortex* 24, 663–676.
- Azzinnari, D., Sigrist, H., Staehli, S., Palme, R., Hildebrandt, T., Lepar, G., Hengerer, B., Seifritz, E., Pryce, C.R., 2014. Mouse social stress induces increased fear conditioning, helplessness and fatigue to physical challenge together with markers of altered immune and dopamine function. *Neuropharmacology* 85, 328–341.
- Barttfeld, P., Uhrig, L., Sitt, J.D., Sigman, M., Jarraya, B., Dehaene, S., 2015. Signature of consciousness in the dynamics of resting-state brain activity. *Proc. Natl. Acad. Sci. USA* 112, 887–892.
- Betz, R.F., Fukushima, M., He, Y., Zuo, X.N., Sporns, O., 2016. Dynamic fluctuations coincide with periods of high and low modularity in resting-state functional brain networks. *NeuroImage* 127, 287–297.
- Boly, M., Massimini, M., Garrido, M.I., Gosseries, O., Noirhomme, Q., Laureys, S., Soddu, A., 2012. Brain connectivity in disorders of consciousness. *Brain Connect* 2, 1–10.
- Britz, J., Van De Ville, D., Michel, C.M., 2010. BOLD correlates of EEG topography reveal rapid resting-state network dynamics. *NeuroImage* 52, 1162–1170.
- Calhoun, V.D., Miller, R., Pearlson, G., Adali, T., 2014. The chronnectome: time-varying connectivity networks as the next frontier in fMRI data discovery. *Neuron* 84, 262–274.
- Chang, C., Glover, G.H., 2010. Time-frequency dynamics of resting-state brain connectivity measured with fMRI. *NeuroImage* 50, 81–98.
- Chen, S., Langley, J., Chen, X., Hu, X., 2016. Spatiotemporal modeling of brain dynamics using resting-state functional magnetic resonance imaging with gaussian hidden markov model. *Brain Connect* 6, 326–334.
- Friston, K., 2002. Beyond phrenology: what can neuroimaging tell us about distributed circuitry? *Annu. Rev. Neurosci.* 25, 221–250.
- Fuertig, R., Azzinnari, D., Bergamini, G., Cathomas, F., Sigrist, H., Seifritz, E., Vavassori, S., Luippold, A., Hengerer, B., Ceci, A., Pryce, C.R., 2016. Mouse chronic social stress increases blood and brain kynurenine pathway activity and fear behaviour: both effects are reversed by inhibition of indoleamine 2,3-dioxygenase. *Brain Behav. Immun.* 54, 59–72.
- Fukuda, M., Vazquez, A.L., Zong, X., Kim, S.G., 2013. Effects of the alpha(2)-adrenergic receptor agonist dexmedetomidine on neural, vascular and BOLD fMRI responses in the somatosensory cortex. *Eur. J. Neurosci.* 37, 80–95.
- Gozzi, A., Schwarz, A.J., 2016. Large-scale functional connectivity networks in the rodent brain. *NeuroImage* 127, 496–509.
- Grandjean, J., Schroeter, A., Batata, I., Rudin, M., 2014a. Optimization of anesthesia protocol for resting-state fMRI in mice based on differential effects of anesthetics on functional connectivity patterns. *NeuroImage* 102 (Pt 2), 838–847.
- Grandjean, J., Azzinnari, D., Seuwen, A., Sigrist, H., Seifritz, E., Pryce, C.R., Rudin, M., 2016a. Chronic psychosocial stress in mice leads to changes in brain functional connectivity and metabolite levels comparable to human depression. *NeuroImage*.
- Grandjean, J., Derungs, R., Kulic, L., Welt, T., Henkelman, M., Nitsch, R.M., Rudin, M., 2016b. Complex interplay between brain function and structure during cerebral amyloidosis in APP transgenic mouse strains revealed by multi-parametric MRI comparison. *NeuroImage* 134, 1–11.
- Grandjean, J., Schroeter, A., He, P., Tanadini, M., Keist, R., Krstic, D., Konietzko, U., Klohs, J., Nitsch, R.M., Rudin, M., 2014b. Early alterations in functional connectivity and white matter structure in a transgenic mouse model of cerebral amyloidosis. *J. Neurosci.* 34, 13780–13789.
- Greicius, M., 2008. Resting-state functional connectivity in neuropsychiatric disorders. *Curr. Opin. Neurol.* 21, 424–430.
- Hindriks, R., Adhikari, M.H., Murayama, Y., Ganzetti, M., Mantini, D., Logothetis, N.K., Deco, G., 2016. Can sliding-window correlations reveal dynamic functional connectivity in resting-state fMRI? *NeuroImage* 127, 242–256.
- Hutchison, R.M., Womelsdorf, T., Gati, J.S., Everling, S., Menon, R.S., 2013. Resting-state networks show dynamic functional connectivity in awake humans and anesthetized macaques. *Hum. Brain Mapp.* 34, 2154–2177.
- Kaiser, R.H., Whitfield-Gabrieli, S., Dillon, D.G., Goer, F., Beltzer, M., Minkel, J., Smoski, M., Dichter, G., Pizzagalli, D.A., 2016. Dynamic resting-state functional connectivity in major depression. *Neuropsychopharmacology* 41, 1822–1830.
- Kalshoff, D., Seehafer, J.U., Po, C., Wiedermann, D., Hoehn, M., 2011. Functional connectivity in the rat at 11.7T: impact of physiological noise in resting state fMRI. *NeuroImage* 54, 2828–2839.
- Karahanoglu, F.I., Van De Ville, D., 2015. Transient brain activity disentangles fMRI resting-state dynamics in terms of spatially and temporally overlapping networks. *Nat. Commun.* 6, 7751.
- Keilholz, S.D., Magnuson, M.E., Pan, W.J., Willis, M., Thompson, G.J., 2013. Dynamic properties of functional connectivity in the rodent. *Brain Connect* 3, 31–40.
- Kuhn, H.W., 2010. The Hungarian method for the assignment problem. In: Jünger, M., Lieblich, T.M., Naddef, D., Nemhauser, G.L., Pulleyblank, W.R., Reinelt, G., Rinaldi, G., Wolsey, L.A. (Eds.), *50 Years of Integer Programming 1958-2008: From the Early Years to the State-of-the-Art*. Springer Berlin Heidelberg, Berlin, Heidelberg, 29–47.
- Kundu, P., Inati, S.J., Evans, J.W., Luh, W.M., Bandettini, P.A., 2012. Differentiating BOLD and non-BOLD signals in fMRI time series using multi-echo EPI. *NeuroImage* 60, 1759–1770.
- Lee, J.H., Durand, R., Gradinaru, V., Zhang, F., Goshen, I., Kim, D.S., Fenno, L.E., Ramakrishnan, C., Deisseroth, K., 2010. Global and local fMRI signals driven by neurons defined optogenetically by type and wiring. *Nature* 465, 788–792.
- Leonardi, N., Van De Ville, D., 2015. On spurious and real fluctuations of dynamic functional connectivity during rest. *NeuroImage* 104, 430–436.
- Leonardi, N., Shirer, W.R., Greicius, M.D., Van De Ville, D., 2014. Disentangling dynamic networks: separated and joint expressions of functional connectivity patterns in time. *Hum. Brain Mapp.* 35, 5984–5995.
- Leonardi, N., Richiardi, J., Gschwind, M., Simioni, S., Annoni, J.M., Schlupe, M., Vuilleumier, P., Van De Ville, D., 2013. Principal components of functional connectivity: a new approach to study dynamic brain connectivity during rest. *NeuroImage* 83, 937–950.
- Li, X., Zhu, D., Jiang, X., Jin, C., Zhang, X., Guo, L., Zhang, J., Hu, X., Li, L., Liu, T., 2014. Dynamic functional connectomics signatures for characterization and differentiation of PTSD patients. *Hum. Brain Mapp.* 35, 1761–1778.
- Lindquist, M.A., Xu, Y., Nebel, M.B., Caffo, B.S., 2014. Evaluating dynamic bivariate correlations in resting-state fMRI: a comparison study and a new approach. *NeuroImage* 101, 531–546.
- Liska, A., Galbusera, A., Schwarz, A.J., Gozzi, A., 2015. Functional connectivity hubs of the mouse brain. *NeuroImage* 115, 281–291.
- Liu, X., Duyn, J.H., 2013. Time-varying functional network information extracted from brief instances of spontaneous brain activity. *Proc. Natl. Acad. Sci. USA* 110, 4392–4397.
- Magnuson, M.E., Thompson, G.J., Pan, W.J., Keilholz, S.D., 2014. Time-dependent effects of isoflurane and dexmedetomidine on functional connectivity, spectral characteristics, and spatial distribution of spontaneous BOLD fluctuations. *NMR Biomed.* 27, 291–303.
- Majeed, W., Magnuson, M., Hasenkamp, W., Schwarb, H., Schumacher, E.H., Barsalou, L., Keilholz, S.D., 2011. Spatiotemporal dynamics of low frequency BOLD fluctuations in rats and humans. *NeuroImage* 54, 1140–1150.
- Manoliu, A., Meng, C., Brandl, F., Doll, A., Tahmasian, M., Scherr, M., Schwerthoffer, D., Zimmer, C., Forstl, H., Bauml, J., Riedl, V., Wohlschlagel, A.M., Sorg, C., 2013. Insular dysfunction within the salience network is associated with severity of symptoms and aberrant inter-network connectivity in major depressive disorder. *Front. Hum. Neurosci.* 7, 930.
- Nasrallah, F.A., Tay, H.C., Chuang, K.H., 2014. Detection of functional connectivity in the resting mouse brain. *NeuroImage* 86, 417–424.
- Power, J.D., Schlaggar, B.L., Petersen, S.E., 2014. Studying brain organization via spontaneous fMRI signal. *Neuron* 84, 681–696.
- Razouf, F., Baltes, C., Mueggler, T., Seuwen, A., Rüssig, H., Mansuy, I., Rudin, M., 2013. Functional MRI to assess alterations of functional networks in response to pharmacological or genetic manipulations of the serotonergic system in mice. *NeuroImage* 74, 326–336.
- Sakoglu, U., Pearlson, G.D., Kiehl, K.A., Wang, Y.M., Michael, A.M., Calhoun, V.D., 2010. A method for evaluating dynamic functional network connectivity and task-modulation: application to schizophrenia. *MAGMA* 23, 351–366.
- Salimi-Khorshidi, G., Douaud, G., Beckmann, C.F., Glasser, M.F., Griffanti, L., Smith, S.M., 2014. Automatic denoising of functional MRI data: combining independent component analysis and hierarchical fusion of classifiers. *NeuroImage* 90, 449–468.
- Schroeter, A., Schlegel, F., Seuwen, A., Grandjean, J., Rudin, M., 2014. Specificity of stimulus-evoked fMRI responses in the mouse: the influence of systemic physiological changes associated with innocuous stimulation under four different anesthetics. *NeuroImage* 94, 372–384.
- Sforzazzini, F., Schwarz, A.J., Galbusera, A., Bifone, A., Gozzi, A., 2014. Distributed BOLD and CBV-weighted resting-state networks in the mouse brain. *NeuroImage* 87, 403–415.
- Shakil, S., Lee, C.H., Keilholz, S.D., 2016. Evaluation of sliding window correlation performance for characterizing dynamic functional connectivity and brain states. *NeuroImage* 133, 111–128.
- Sheline, Y.I., Price, J.L., Yan, Z., Mintun, M.A., 2010. Resting-state functional MRI in depression unmasks increased connectivity between networks via the dorsal nexus. *Proc. Natl. Acad. Sci. USA* 107, 11020–11025.
- Thompson, G.J., Merritt, M.D., Pan, W.J., Magnuson, M.E., Grooms, J.K., Jaeger, D., Keilholz, S.D., 2013. Neural correlates of time-varying functional connectivity in the rat. *NeuroImage* 83, 826–836.
- Van de Ville, D., Britz, J., Michel, C.M., 2010. EEG microstate sequences in healthy humans at rest reveal scale-free dynamics. *Proc. Natl. Acad. Sci. USA* 107, 18179–18184.
- Zerbi, V., Grandjean, J., Rudin, M., Wenderoth, N., 2015. Mapping the mouse brain with rs-fMRI: an optimized pipeline for functional network identification. *NeuroImage* 123, 11–21.